ACS MATERIALS LETTERS

www.acsmaterialsletters.org

Low-Temperature Plasma-Enhanced Atomic Layer Deposition of ZnMgO for Efficient CZTS Solar Cells

Xin Cui, Kaiwen Sun,* Jialiang Huang, Heng Sun, Ao Wang, Xiaojie Yuan, Martin Green, Bram Hoex,* and Xiaojing Hao*

Cite This: *ACS Materials Lett.* 2023, 5, 1456−1465

Read Online

ACCESS | Metrics & More | Article Recommendations | Supporting Information

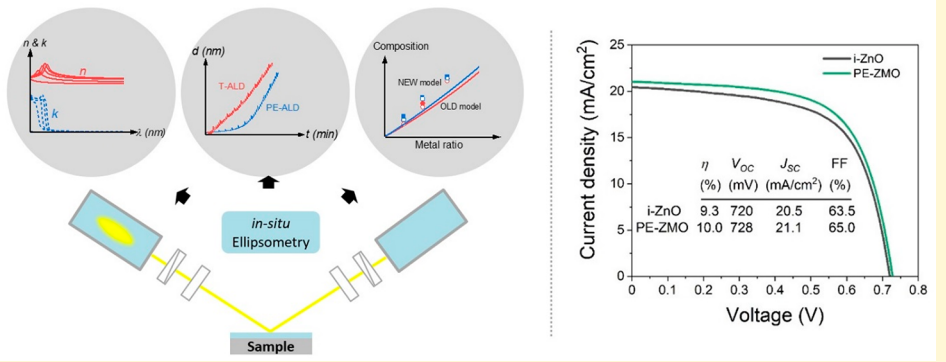

ABSTRACT: **Cu_2ZnSnS_4 (CZTS) solar cells are an emerging photovoltaic technology owing to their earth abundance, all-dry processability, and environmental friendliness. Further power conversion efficiency enhancement of the Cd-free CZTS device necessitates the substitution of traditionally used intrinsic ZnO by an alternative wide-band-gap window layer. Here, we demonstrate deposition of a ZnMgO window layer of controlled thickness, composition, and electro-optical properties by atomic layer deposition (ALD). The amorphous ZnMgO deposited at low temperature down to 100 °C using plasma-enhanced ALD showed smoothness superior to that of high-temperature plasma-enhanced ALD and doping density comparable to that of high-temperature thermal ALD but with a much lower electron affinity. The overall charge carrier recombination at the CZTS/ZnSnO/ZnMgO region was reduced due to the optimized ZnMgO conduction band minimum, thus reducing the V_{OC} value and fill factor loss for a CZTS solar cell. In addition, the thinner- and larger-band-gap ZnMgO was believed to reduce the parasitic absorption, improving the J_{SC} value and boosting the efficiency to 10%.**

Environmentally friendly and earth-abundant Cu_2ZnSnS_4 (CZTS) solar cells hold the potential as a top cell in tandem solar cells to couple with the current state-of-the-art low-band-gap Si solar cell, owing to the wide band gap of the CZTS absorber (~1.55 eV). A Cd-free CZTS solar cell with a structure of Mo/CZTS/ZnSnO/i-ZnO/ITO demonstrated an efficiency of 9.3% in our previous work.[1] It was further boosted to 10.2% with the passivation of the CZTS/ZnSnO heterojunction interface by atomic layer deposited Al_2O_3 (Mo/CZTS/Al_2O_3/ZnSnO/i-ZnO/ITO).[2] A promising next step to enhance the power conversion efficiency (PCE) of CZTS solar cells is to optimize buffer/window structures, which allows for more flexibility in the optical and electrical engineering of the device.

A 50−70 nm thick sputtered intrinsic ZnO (i-ZnO) layer, also known as a window layer, is commonly employed in CZTS champion devices.[3] The presence of i-ZnO increases the shunt resistance by blocking shunt pathways such as pinholes, cracks, and voids, thus preventing electrical inhomogeneities and thereby improving the fill factor (FF) of the solar cell.[4] The function of i-ZnO in preventing the shunting path is in

Received: December 23, 2022
Accepted: April 5, 2023

https://doi.org/10.1021/acsmaterialslett.2c01203
ACS Materials Lett. 2023, 5, 1456−1465

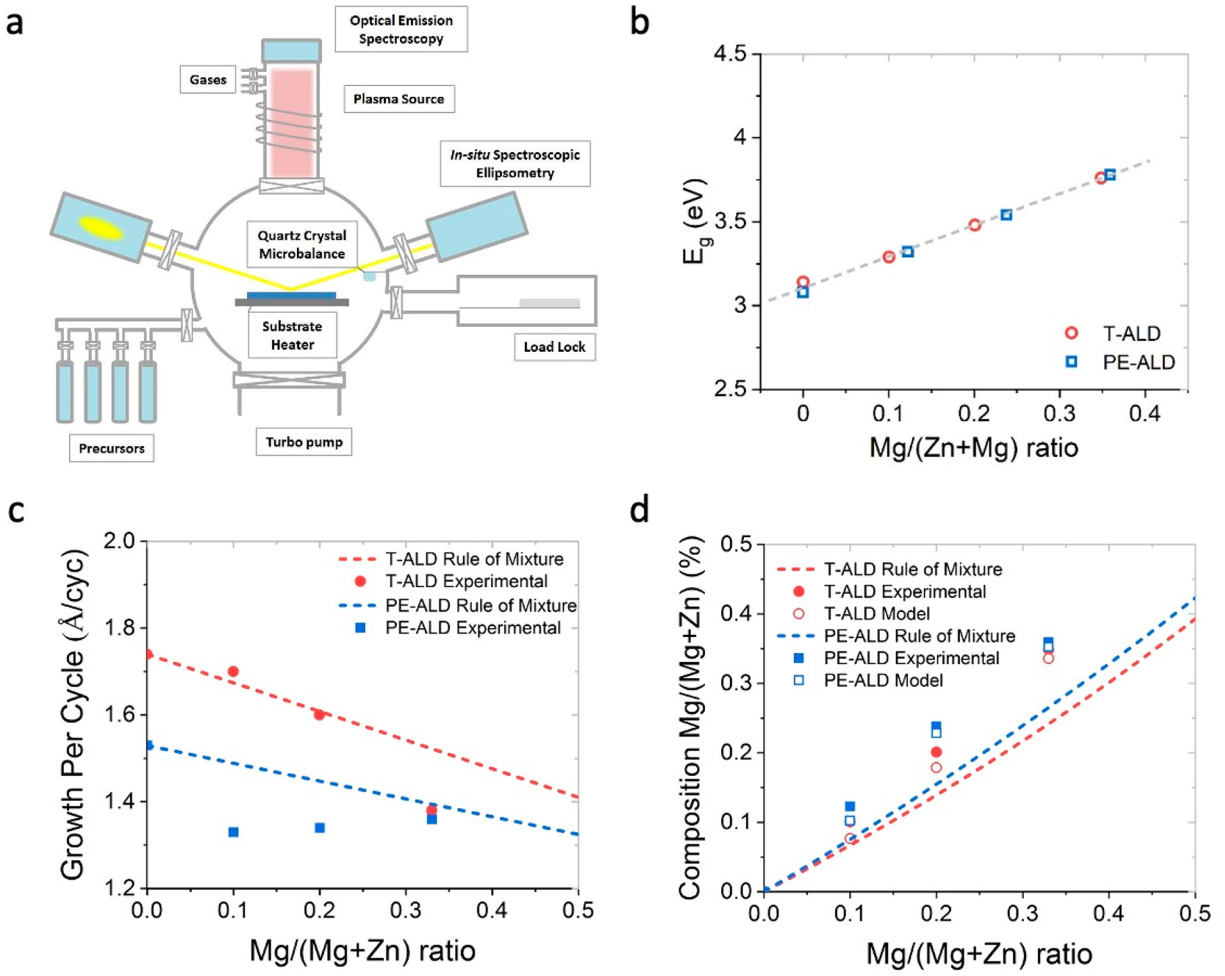

Figure 1. (a) Schematic representation of the Fiji G2 ALD system with *in situ* spectroscopic ellipsometry used for the thermal ALD and PE-ALD deposition in this work. (b) Growth behavior of a ZnMgO film via T-ALD and PE-ALD at 150 °C. (c) Variations in growth per cycle (GPC; circles and squares) of ZMO films as a function of the ALD subcycle ratio compared to the trends calculated from the rule of mixture (dashed lines). (d) Experimental composition (filled circles and squares) determined from ICP-OES of the ZMO films as a function of ALD subcycle ratio compared to the trends calculated from the rule of mixture (dashed lines) and a modified model (open circles and squares).

particular beneficial when the CZTS absorber layer is coated with a chemical-bath-deposited CdS buffer layer, which generally has poor conformality compared to a ZnSnO buffer layer deposited by atomic layer deposition (ALD).[5] However, in the case of an ALD ZnSnO buffer layer, a thick i-ZnO layer might not be necessary and can be replaced with alternative wider-band-gap thin layers to reduce the parasitic absorption and hence improve the short-circuit current density (J_{SC}). Another reason for replacing the i-ZnO window layer is to reduce the high carrier recombination at the associated interface, which is supposed to stem from an unfavorable conduction band gap offset (CBO), interface defects, and sputter-induced damage on the surface from the energetic sputtering deposition of ZnO.[4,6,7] It was demonstrated that the carrier recombination rate can be suppressed through the optimization of the CBO not only between the buffer and absorber but also between the window layers and absorber in $Cu(In,Ga)(S,Se)_2$ (CIGSSe) solar cells.[8] Apart from that, doping the window layer is a critical factor contributing to the enhancement of V_{OC} and FF, as demonstrated in chalcogenide devices.[7,9]

A potential window layer satisfying all the above requirements is ZnMgO (ZMO) with tunable electro-optical properties, with a demonstrated potential with CIGS and CdTe solar cells:[10,11] for example, Solar Frontier achieved the successful integration of ZMO coupled with a Zn(O,S,OH) buffer layer in their record CIGS device with a 23.35% efficiency.[11] ZMO can be deposited by several techniques, such as sputtering,[12] pulsed-laser deposition (PLD),[13] metal–organic chemical vapor deposition (MOCVD),[14] and atomic layer deposition (ALD).[15] The band gap of ZMO can be tuned from 3.3 eV (ZnO) to 7.7 eV (MgO),[12,16] and this shift primarily results from a change in the position of the conduction band compared to the vacuum level.[17] However, a substantial decrease in the maximal achievable conductivity is observed with higher Mg composition,[12,18] which limits the exploration of doping ZMO as a strategy to improve the device performance. Although ZnMgO can be degenerately doped to/as n-type by substitutional doping on the cation lattice with Al, Ga, or B,[19,20] more flexibility on intrinsic doping of ZnMgO can be obtained via thermal ALD (T-ALD) and plasma-enhanced atomic layer deposition (PE-ALD). Thermal ALD for deposition of a window layer could benefit device performance in terms of mitigation of plasma damage[21] and better control over nanostructure and composition.[22] In contrast, PE-ALD gives a high tunability for the intrinsic

https://doi.org/10.1021/acsmaterialslett.2c01203
ACS Materials Lett. 2023, 5, 1456−1465

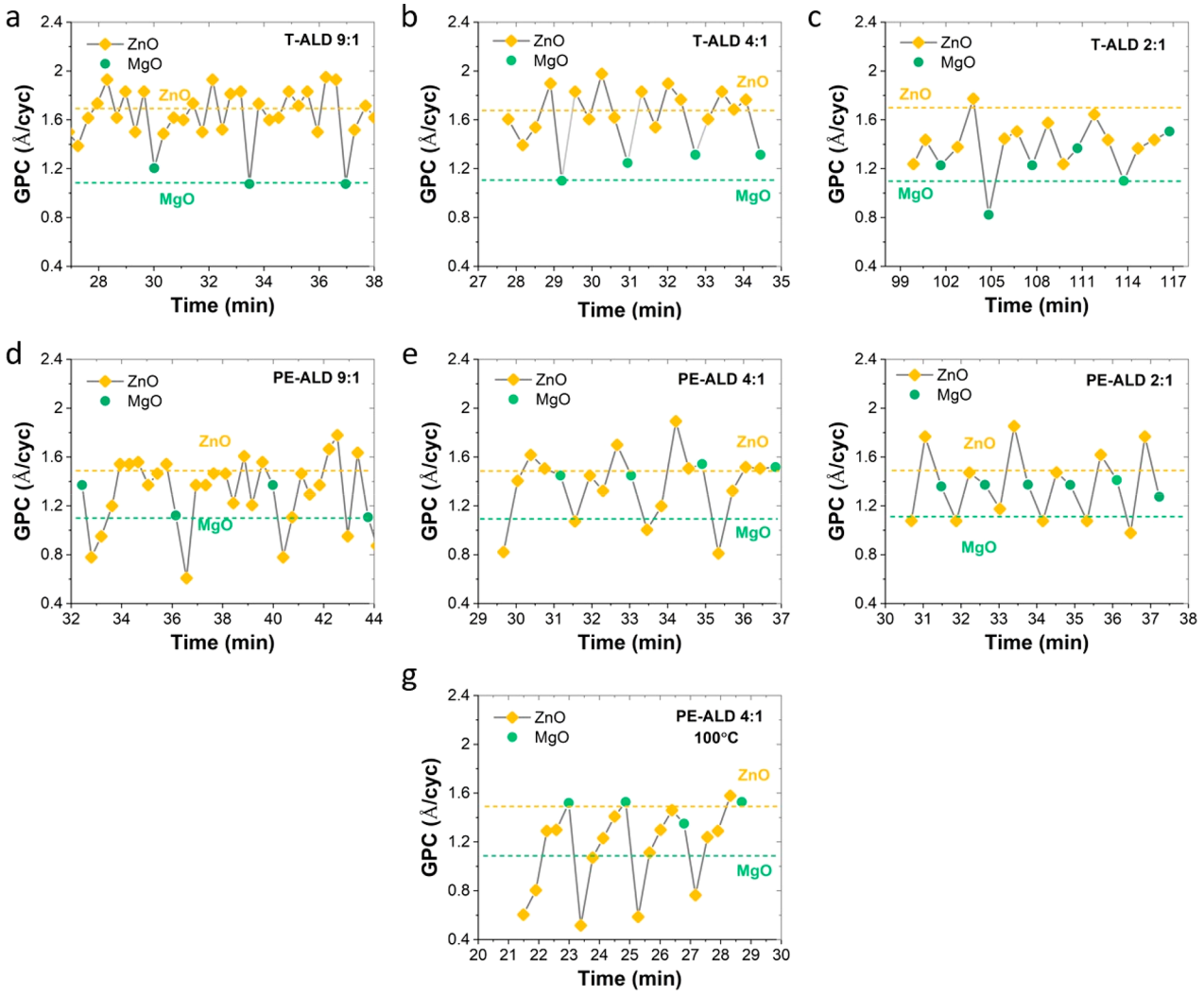

Figure 2. GPC of consecutive ZnO and MgO subcycles using (a–c) T-ALD and (d–g) PE-ALD as measured by *in situ* ellipsometry. The dashed lines indicate the GPC for pure ZnO and MgO.

doping of zinc oxides with a much wider range of resistivity and carrier concentration.[23,24] However, high-temperature PE-ALD may result in higher film roughness, degrading the device performance, causing us to be more focused on developing low-temperature PE-ALD processes.[25]

In this work, we employed *in situ* ellipsometry to monitor the growth behavior and optical properties and to predict the composition of the ZMO films by a modified rule of mixtures (ROM) model, thereby facilitating the accurate control and tunability of material properties in real time. T-ALD and PE-ALD were used to explore the ZMO films with a broad range of electro-optical properties. We demonstrate that the deposition temperature of ZMO layers that results in the best device performance can be reduced to 100 °C using PE-ALD. It shows that a reduced cliff-like CBO between the buffer and window layer together with moderate doping of ZMO contributed to the suppressed charge carrier recombination at the heterojunction. This optimized ZMO window layer processed by low-temperature PE-ALD simultaneously facilitates reducing the parasitic loss and resistance loss and improving the CBO, thereby enhancing the efficiency to 10%.

Optical Properties and Growth Behaviors. The ZnMgO ternary films were deposited by tuning the ZnO:MgO ratio with a supercycle approach, and the sequence of the two processes is illustrated in Figure S1. Here, thermal ALD is abbreviated "T-ALD", and plasma-enhanced ALD is abbreviated "PE-ALD". A typical supercycle consisted of alternating m cycles of the ZnO process followed by one cycle of the MgO process. The desired thickness was achieved by looping the ALD supercycles. Both T-ALD and PE-ALD were used to deposit the ZMO films with various compositions by tuning the Zn/Mg pulse ratio from 9:1 to 2:1. To monitor the optical properties and growth behavior and to predict the composition of the ZMO films, *in situ* spectroscopic ellipsometry (SE) in the ALD system was used to perform the measurement, as shown in Figure 1a. The absorption coefficient was then calculated from the well-known relation $\alpha = 4\pi k/\lambda$, where k represents the imaginary part of the complex dielectric constant and λ is the light wavelength. Figure S2 shows the refractive index (n) and extinction coefficient (k) values extracted from SE as a function of the photon energy for the different ZMO film compositions. Therefore, the band gap was acquired by using a Tauc plot for ZMO films deposited by T-ALD and PE-ALD, as shown in Figure 1b. The band gap of ZMO increases almost linearly from ~3.2 to ~3.8 eV as a function of Mg content in the range of $0 \leq \mathrm{Mg}/(\mathrm{Mg+Zn}) \leq$

https://doi.org/10.1021/acsmaterialslett.2c01203
ACS Materials Lett. 2023, 5, 1456–1465

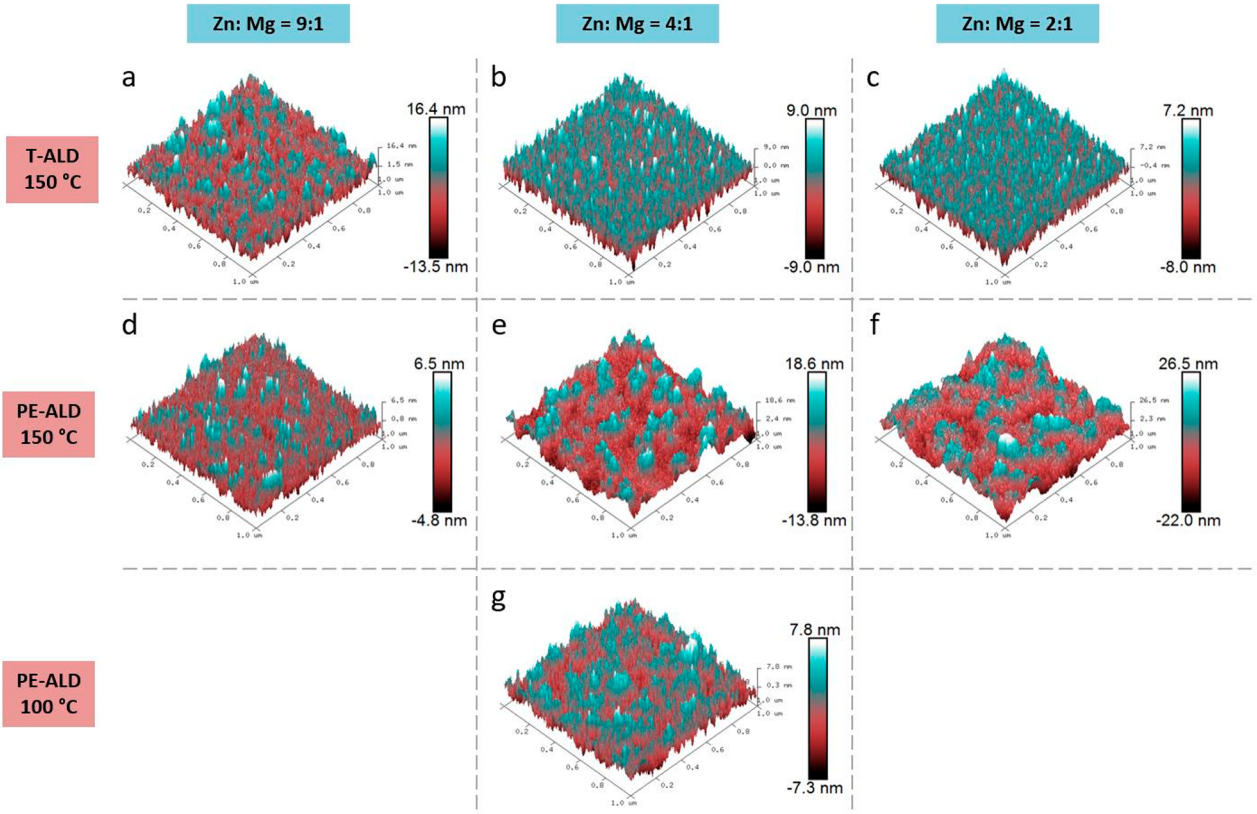

Figure 3. Atomic force microscope (AFM) morphology of various ZMO thin films deposited through (a–c) T-ALD at 150 °C, (d–f) PE-ALD at 150 °C, and (g) PE-ALD at 100 °C.

0.36, for both T-ALD and PE-ALD ZMO films. The band gap of ZMO compounds can be easily tuned by varying the Mg content, in good agreement with previously published results.[12,19]

The growth behavior and growth rate of ternary ZMO can be well understood by using *in situ* SE. As seen in Figure S3, the dynamic SE data show that T-ALD-processed films have a distinct incubation period of ∼40–50 cycles before a steady-state growth per cycle (GPC) is achieved. This nucleation behavior is similar to the growth of pure ZnO, which shows that ZnO by T-ALD exhibits an island-like growth on Si at the initial stage.[26] In contrast, a linear ALD growth behavior without a distinct nucleation delay was observed for the PE-ALD process. The tremendous changes in the nucleation stage could be attributed to the higher oxidation strength of the oxygen plasma compared to water, which leads to the rapid oxidation of the c-Si substrate, resulting in a higher GPC at the initial stage.[27] The average steady-state GPC of the ZMO films deposited by T-ALD decreased with an increasing percentage of MgO cycles, while the average GPC of PE-ALD films was almost constant and independent of the subcycle ratio, as shown in Figure 1c and summarized in Table S1. We also compared the experimental GPC with the expected GPC from the ROM model,[28] which assumes the materials grow independently from one another

$$\mathrm{GPC} = \mathrm{CR}_{\mathrm{MgO}}\mathrm{GPC}_{\infty,\mathrm{MgO}} + (1 - \mathrm{CR}_{\mathrm{MgO}})\mathrm{GPC}_{\infty,\mathrm{ZnO}} \quad (1)$$

where $\mathrm{GPC}_{\infty,x}$ and CR_x refer to the growth rate of the pure binary process and the fraction of the cycle of metal oxide x in the supercycle process, respectively. However, some of the experimental GPC values and expected values from the ROM are not in good agreement, as described in Figure 1c. To better understand the deviations between experimental and ROM GPC values, we further checked the dynamic GPC values of each subcycle at the steady growth stage. GPC values of 1.7 and 1.1 Å were determined for pure ZnO and MgO processes and plotted as dashed lines in Figure 2a–g. For both T-ALD and PE-ALD, the first 2–3 cycles of ZnO after MgO were observed to have a significantly lower GPC than for the binary process, which points toward a nucleation delay when switching from MgO to ZnO subcycle. This effect could be related to the reduced reaction site density of the Mg–O terminated surface compared to Zn–O in the binary process.[29] In contrast, the GPC of MgO after the ZnO subcycle was higher than that in the binary process due to the higher density of the reaction sites or/and enhanced chemisorption on the Zn–O surface. Nevertheless, the reaction mechanism is different when metal precursors are paired with H_2O or O_2 plasma coreactant. For the first ZnO cycle after MgO, there is a deficit of ∼40% relative to the value obtained from the binary process for PE-ALD ZMO films, which is larger than the deficit of ∼20% for T-ALD ZMO films. In contrast, the growth gain of the MgO cycle was higher in the case of the PE-ALD process (20–30%) than in the T-ALD process (0–10%). By comparing the films with Zn/Mg cycle ratios from 9:1 to 2:1, it can be observed that the nucleation delays and reaction kinetics play a more dominant role for higher Zn/Mg cycle ratios. Hence, this could explain the enhanced deviations of GPC from the ROM value for PE-ALD films with lower Mg doping, as illustrated in Figure 1c.

https://doi.org/10.1021/acsmaterialslett.2c01203
ACS Materials Lett. 2023, 5, 1456–1465

Prediction of Composition. Apart from the growth behavior, a precise prediction of the film composition is another challenge in developing the supercycle processes.[30] A modified ROM model is then introduced in this work to predict the *in situ* composition. Generally, the expected composition of the films can be calculated from the rule of mixtures as

$$\text{composition}_{\text{Mg,ROM}} = \frac{\rho_{\text{MgO}}\text{GPC}_{\infty,\text{MgO}}\text{CR}_{\text{MgO}}}{\rho_{\text{MgO}}\text{GPC}_{\infty,\text{MgO}}\text{CR}_{\text{MgO}} + \rho_{\text{ZnO}}\text{GPC}_{\infty,\text{ZnO}}(1 - \text{CR}_{\text{MgO}})} \quad (2)$$

where $\rho_{M_yO_x}$ is the atomic density of the binary materials. Figure 1d displays the relative Mg concentration (Mg/(Zn +Mg)) as a function of the subcycle ratio determined by ICP-OES compared to the trends calculated from the ROM. When $\text{GPC}_{\infty,x}$ of the pure binary process was used to estimate the composition of the ternary films, it led to a significant error because the ternary films contain less or more of the binary components than expected caused by the nucleation delay effects. Therefore, a more accurate model was required to estimate the composition using an ALD supercycle recipe. In this work, $\text{GPC}_{\infty,x}$ was replaced by the average dynamic $\text{GPC}_{\text{real},M_yO_x}$ in the ternary process to express the composition of the deposited films as

$$\text{composition}_{\text{Mg}} = \frac{\dot{\sigma}_{\text{Mg}}\text{CR}_{\text{MgO}}}{\dot{\sigma}_{\text{Mg}}\text{CR}_{\text{MgO}} + \dot{\sigma}_{\text{Zn}}(1 - \text{CR}_{\text{ZnO}})} \quad (3)$$

Where $\dot{\sigma}_{\text{Mg}}$ and $\dot{\sigma}_{\text{Zn}}$ are represented as areal atomic densities of Mg and Zn deposited during each ALD cycle in units of atoms/(cm^2 cycle). $\dot{\sigma}_{\text{M}}$ can be described by applying the real-time GPC measured by *in situ* ellipsometry

$$\dot{\sigma}_{\text{M}} = \frac{\rho_{M_yO_x}\text{GPC}_{\text{real},M_yO_x}N_A y}{\text{MW}_{M_yO_x}} \quad (4)$$

The resulting composition from the real-time $\text{GPC}_{\text{real},M_yO_x}$ model was found to align well with the experimental value, as shown in Figure 1d. This model helps to quantify the composition when developing a supercycle recipe. Furthermore, this model of predicting the composition of ALD ternary materials could be easily applied to ALD quaternary materials or a more complex system.

Material and Electrical Properties. The surface morphology and roughness of ~40 nm ZMO thin films were then investigated and correlated with the crystalline structure. The resonant Raman results in Figure S4 show the successful incorporation of Mg into ZnO. For both T-ALD- and PE-ALD-processed ZMO films, a monotonous increase in the frequency of the LO main peaks at around 600 cm^{-1} with Mg alloying can be observed.[31] This is related to the increased lattice constant of ZMO film with increasing Mg concentration, which indicates the successful incorporation of Mg into the ZnO wurtzite structure. Figure 3 presents atomic force microscope (AFM) images of ZMO films deposited on soda-lime glass (SLG) substrates by T-ALD and PE-ALD with various compositions. At first glance, the T-ALD ZMO films exhibited superior smoothness and a lower roughness than the PE-ALD ZMO films. This could be related to the crystalline growth with a different preferred orientation, as is evident from the grazing incidence X-ray diffraction (GIXRD) pattern in Figure S5a,b. Previous reports have shown that the variation of surface roughness was correlated with the crystallinity and crystal size of the films.[32] Specifically, ZMO films grown by T-ALD at 150 °C (T-ZMO 150) have a preferred orientation along (100), while the ZMO deposited by PE-ALD at 150 °C (PE-ZMO 150) were oriented along the (002) direction. Thus, T-ZMO 150 films tend to be less rough due to the formation of laterally oriented grains. The T-ZMO 150 films have root-mean-square (rms) surface roughnesses of 4.0, 2.5, and 2.1 nm for Zn/Mg pulse ratios of 9:1, 4:1 and 2:1, respectively. A smoother surface was obtained for ZMO films with a higher Mg concentration. As indicated by the GIXRD results of ZMO in Figure S5a, the (002) peak intensity decreased with increasing Mg incorporation. Therefore, the roughness decreases as a result of this prohibited growth of grains perpendicular to the substrate surface. On the other hand, the roughness shows an opposite trend for PE-ALD ZMO films, where rms values of 1.5, 5.1, and 7.0 nm were found for ZMO with Zn/Mg pulse ratios of 9:1, 4:1 and 2:1, respectively, which correlated with the decreased (100) and (101) orientations. However, a lower roughness was obtained for the PE-ALD ZMO film deposited at 100 °C (PE-ZMO 100), as it turned out to be amorphous with only broad peaks. Therefore, T-ZMO 150 and PE-ZMO 100 films were smoother than PE-ZMO 150 for the Zn/Mg ratio of 4:1.

The variation in the material structure directly leads to a significant change in the electrical properties of the films, as demonstrated in Figure S5c,d. For T-ALD ZMO films, the resistivity was found to increase with the Mg/(Zn+Mg) ratio as a result of the decreased product of carrier concentration and carrier mobility. The decrease in carrier concentration has previously been attributed to an increasing donor activation energy due to a larger effective mass band structure change[33] and a lowering of the active donor concentration due to composition enrichment.[34] Furthermore, when the Mg content becomes higher than 0.2, the Hall signal can hardly be detected based on the measurement configuration used due to the large resistivity of the thin films. Similarly, PE-ALD ZMO films deposited at 150 °C demonstrated a high resistivity, which is beyond the detection limit of our Hall setup. The different electrical properties could be correlated with the elemental concentration change in the ZMO films determined from high-resolution XPS measurements, as shown in Figure S6. The atomic ratios of O/(Zn+Mg) in the T-ZMO 150 and PE-ZMO 150 films were determined to be 0.97 and 0.99, respectively, by evaluating the O 1s, Zn $2p_3$, and Mg 1s peak areas. This confirms the formation of more stoichiometric films when the O_2 plasma was used as the coreactant. Another noticeable phenomenon was the discrepancy in O_I/O_{II} ratio, which represents the ratio of M-O-M species to nonlattice oxygen. The ratio value for PE-ZMO was found to be 1.36 while that for T-ZMO was 1.25; hence, the PE-ZMO 150 film possessed a higher amount of metal oxide lattice species and a lower density of oxygen deficiency. Oxygen vacancies are believed to be generally associated with n-type conductivity in doped Zn oxides.[23,35] Thus, the PE-ALD-processed ZMO films possessed enhanced resistivity due to a lower oxygen deficiency. In contrast, the resistivity of PE-ZMO 100 decreased to 23 Ω cm compared to PE-ZMO 150 but was slightly smaller than the 47 Ω cm of T-ZMO 150 film. Even though the resistivity of the two films was in the same order, PE-ALD ZMO had a lower electron concentration than T-ALD ZMO (9.3×10^{15} vs $5.5 \times$

https://doi.org/10.1021/acsmaterialslett.2c01203
ACS Materials Lett. 2023, 5, 1456−1465

Table 1. Corresponding Values of Photovoltaic Parameters of the Champion CZTS Solar Cells with Different ZMO Window Layers Deposited from T-ALD and PE-ALD at Different Temperatures

cell	V_{OC} (mV)	J_{SC} (mA cm^{-2})	FF (%)	eff (%)	R_s (Ω cm^2)	R_{sh} (Ω cm^2)	J_0 (mA cm^{-2})
T-ZMO 150	684	17.7	58.5	7.09	0.98	360	7.74×10^{-3}
PE-ZMO 150	700	18.7	57.1	7.47	0.80	268	3.68×10^{-3}
PE-ZMO 100	710	18.4	59.2	7.76	0.71	451	1.34×10^{-3}

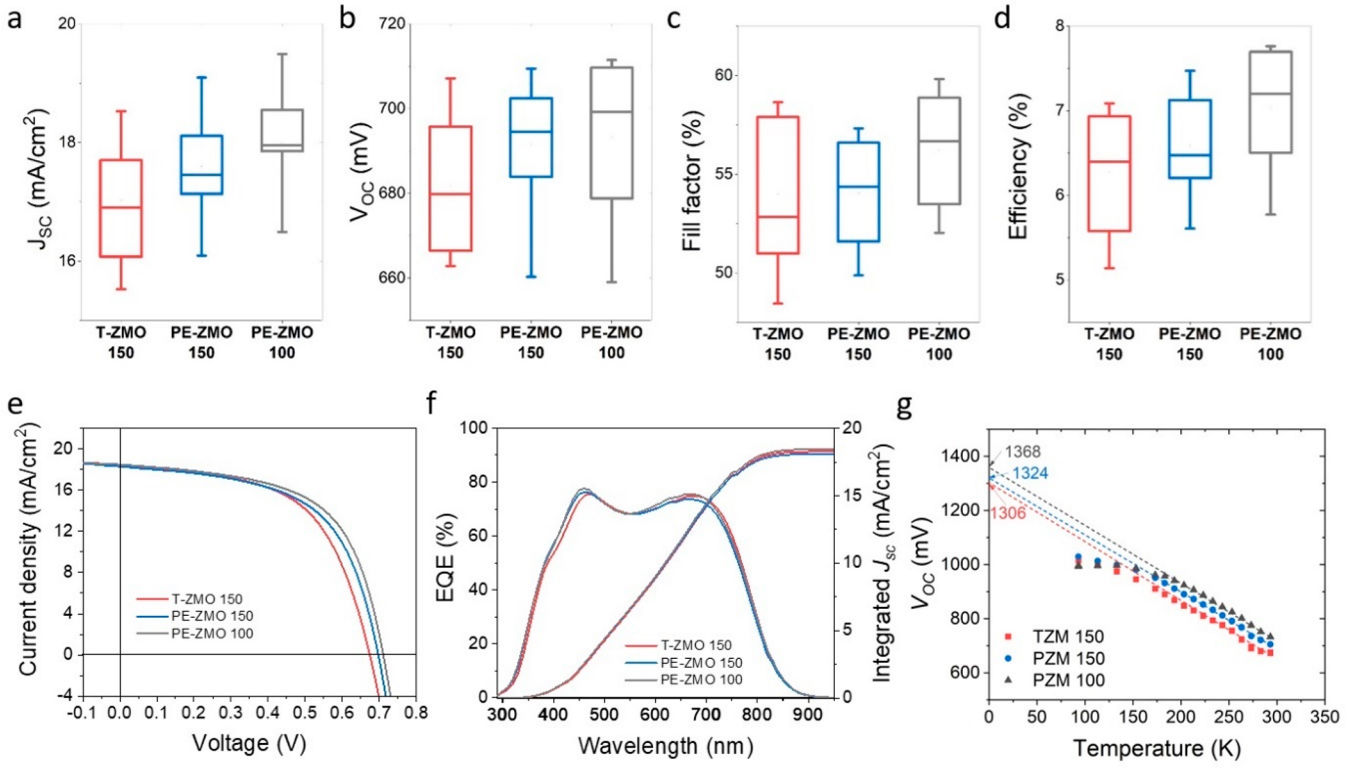

Figure 4. (a–d) Box plots of the photovoltaic parameters of CZTS cells. (e) J–V characteristics, (f) EQE, and (g) V_{OC} as a function of temperature (T) for the best CZTS device with ZMO window layers deposited from T-ALD and PE-ALD at different temperatures. The Zn/Mg pulse ratio was kept as 4:1. Ten CZTS solar cells were fabricated per experimental condition.

10^{16} cm^{-3}) but a much higher mobility (29 vs 2.4 cm^2 V^{-1} s^{-1}). The increase in Hall mobility with decreased temperature by PE-ALD may be closely related to the evolution of the microstructure from polycrystalline films to nanocrystalline films as shown in Figure S5b, which may be the result of fewer oxygen vacancies.

Photovoltaic Performance. Having investigated the growth behavior, composition, and optoelectrical properties of the ZMO films, we employed them as window layers in CZTS solar cells (Table 1). A control device with a sputtered i-ZnO window layer (50 nm thick) was prepared for the composition batch. Experimental devices with T-ALD films deposited at 150 °C were labeled as ZMO 2-1, ZMO 4-1, and ZMO 9-1 for the Zn/Mg pulse ratios of 2:1, 4:1, and 9:1, respectively, while the thickness was kept constant at 10 nm. Each group had ten devices, except for the ZMO 9-1 series, where the very low efficiency cells were excluded in the box plots. ZMO 9-1 film with a low resistivity of 0.1 Ω cm was too conductive to block shunt pathways, thereby deteriorating FF and leading to a low yield (3 points demonstrated). Comparing the photovoltaic characteristics in Figure S7a, the ZMO 2-1 and ZMO 4-1 devices demonstrated slightly higher V_{OC} values when compared to sputtered i-ZnO devices. The higher V_{OC} can be attributed to the band alignment change of the window layer, which will be discussed later. Apart from this, the ZMO 4-1 and ZMO 2-1 devices had slightly higher J_{SC} values than the control device, which is mainly due to higher quantum efficiency in the short-wavelength range, as can be seen in the external quantum efficiency (EQE) curves shown in Figure S8. This could be explained by the reduced parasitic optical loss through higher transparency of the ZMO ($3.7 > E_g > 3.4$ eV) film compared to the reference i-ZnO ($E_g = 3.3$ eV) window layer and much thinner window layer applied in the solar cell (10 nm ALD ZMO vs 50 nm i-ZnO). However, all of the ALD-ZMO devices showed a relatively poor power conversion efficiency (PCE), where the lower FF mainly dominates. We also investigated the effects of thickness on the device performance by fixing the Zn/Mg pulse ratio as 4:1. Although a better FF can be achieved by using thicker (30 nm) ZMO layers, the drop in V_{OC} was still significant, as shown in Figure S7b,c. The average and best efficiencies of the thinner ZMO device were still higher than that those of the thicker device. For the ZMO 2-1 device, a photocurrent blocking behavior was observed with a strongly reduced FF along with a decreased R_{sh} and increased R_s, which indicated the existence of charge recombination and increased contact resistance. Even though the ZMO 4-1 device with an Mg/(Mg+Zn) content of

https://doi.org/10.1021/acsmaterialslett.2c01203
ACS Materials Lett. 2023, 5, 1456–1465

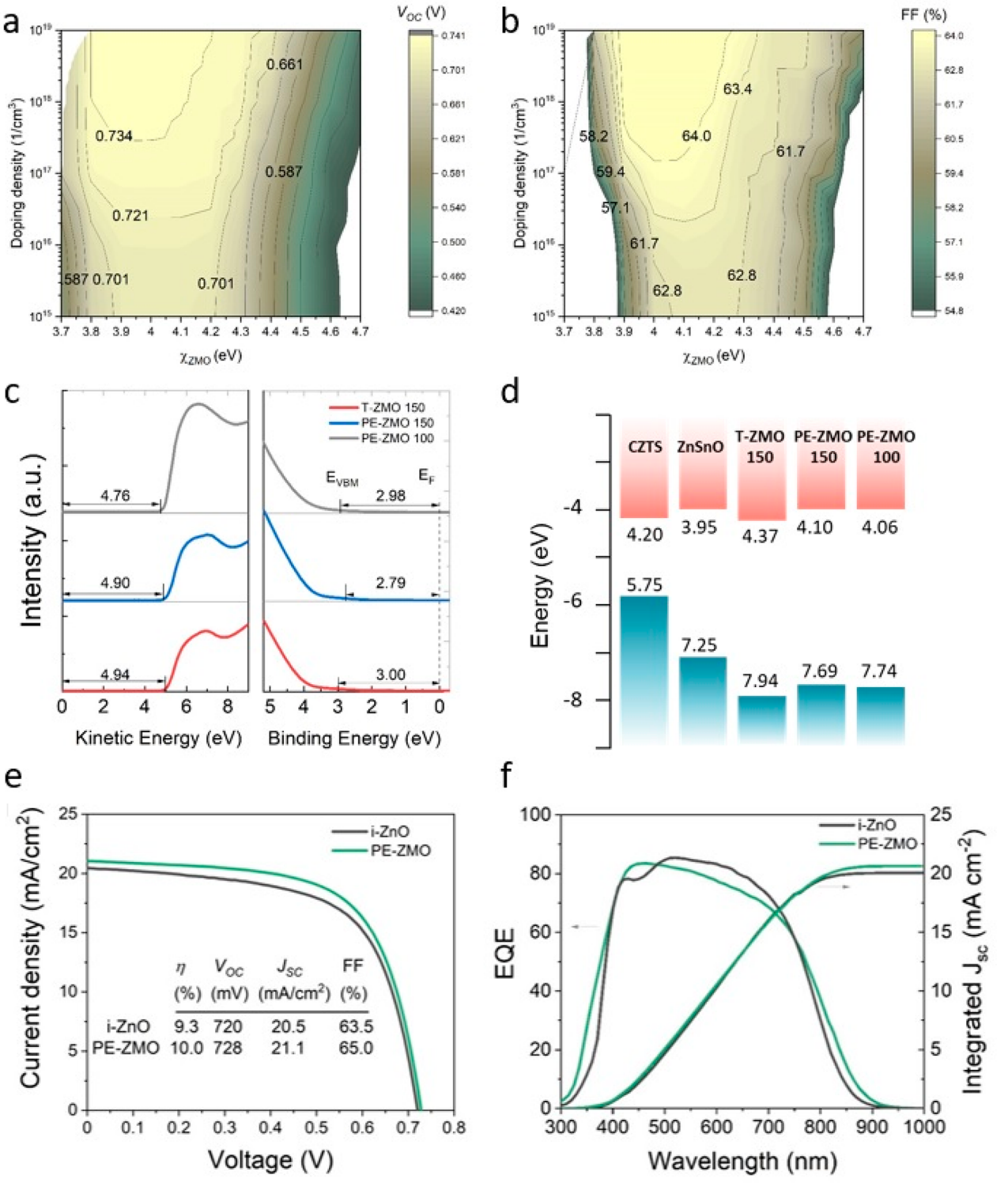

Figure 5. Calculated contour plots of (a) open-circuit voltage, (b) fill factor for CZTS/ZnSnO/ZnMgO devices with the variation of ZMO properties, (c) UPS spectra, and (d) band diagram of ZnMgO thin films synthesized from T-ALD and PE-ALD under different conditions. (e) *J*–*V* characteristics and (f) EQE of the champion CZTS/ZTO/PE-ZMO solar cell with an antireflection coating by using a PE-ZMO window layer with a Zn/Mg pulse ratio of 4:1 deposited at 100 °C.

~0.2 demonstrated a higher FF close to that of the control device, there is still room for further improvement.

PE-ALD processed ZMOs have different optoelectrical properties compared to thermal ALD processed ZMO as previously mentioned; thus, they were further employed as a window layer in CZTS devices. Here, T-ZMO 150, PE-ZMO 150, and PE-ZMO 100 with the same pulse ratio of 4:1 were used for comparison. It is shown in Figure 4a–d that the corresponding photovoltaic parameters of PE-ZMO 100 devices were increased compared to PE-ZMO 150 and were better than T-ZMO 150. The higher performance of the PE-ZMO devices mainly comes from improved V_{OC} and J_{SC}.

https://doi.org/10.1021/acsmaterialslett.2c01203
ACS Materials Lett. 2023, 5, 1456–1465

Figure 4e,f depicts the $J-V$ characteristics and EQE, respectively, for the best CZTS device with different window layers. The J_{SC} integrated from EQE agreed with the J_{SC} from the $J-V$ curve. EQE in the wavelength region of 350−450 nm was notably enhanced when PE-ZMO 100 (3.59 eV) and PE-ZMO 150 (3.68 eV) with an enlarged band gap were used, leading to increased J_{SC}. However, the FF of the PE-ZMO 150 devices dropped compared to the T-ZMO 150 devices, probably due to the large roughness of the film, which led to decreased shunt resistance. An impressive enhancement of average V_{OC} was observed from 684 mV for T-ZMO 150 devices to 700 mV for PE-ZMO 100 and PE-ZMO 150 devices, which could be related to the decreased carrier recombination through an optimized deposition process. Therefore, V_{OC} as a function of temperature was examined, and the activation energy of recombination (E_a) was estimated, as shown in Figure 4g. E_a is defined as qV_{OC} at a temperature of 0 K. E_a would be equivalent to E_g in a p-type absorber if recombination in the space charge region or the neutral bulk was dominant. In this case, E_a of all the devices was estimated to be 1306−1368 mV, which was lower than E_g of the CZTS absorber. It was therefore implied that interfacial recombination was dominant. The device with the PE-ZMO 100 layer had the highest E_a, indicating the recombination rate at the CZTS/ZTO/ZMO region was minimized.

To confirm this, the theoretical effect of the electron affinity and doping of ZMO on device performance was examined by SCAPS simulation[36] with the input parameters summarized in Table S2. Figure 5a,b consequently describes the simulated FF and V_{OC} as a function of the electron affinity (χ) and doping density of the ZMO layer. It is evident that χ_{ZMO} was optimized in a region from approximately 3.80 to 4.25 eV for increased FF and V_{OC}. Within this range, increased doping density could also lead to an even higher photovoltaic performance because of the enhanced built-in potential across the CZTS/ZTO/ZMO p−n junction. It demonstrates that V_{OC} values over 730 mV can be achieved, provided the interface offsets and doping are properly engineered. We then check the band alignments experimentally by applying ultraviolet photoelectron spectroscopy (UPS) measurements on ZMO films. Figure 5c shows an overlay of the UPS spectra for the ZMO layers where the valence band maximum (VBM) relative to the Fermi energy level (E_F) can be determined from the well-established method of extrapolating the valence density of states to zero density. The VBMs estimated from the valence band spectra for T-ZMO 150, PE-ZMO 150, and PE-ZMO 100 samples were 3.00 ± 0.1, 2.79 ± 0.1, and 2.98 ± 0.1 eV below E_F, respectively. Once the VBM was determined, the conduction band minimum (CBM) of ZMOs can be obtained by adding the band gaps of T-ZMO 150 (3.57 eV), PE-ZMO 150 (3.59 eV), and PE-ZMO 100 (3.68 eV) determined from the optical measurements in Figure S9. Herein, the band diagrams at the heterojunction for CZTS/ZTO/ZMO are depicted in Figure 5d. As expected, the PE-ZMOs demonstrated a higher VBM compared to the T-ZMO. The CBOs at ZTO/ZMO were then inferred according to Anderson's rule and were found to be −0.09 ± 0.1, −0.15 ± 0.1, and −0.42 ± 0.1 eV for PE-ZMO 100, PE-ZMO 150, and T-ZMO 150, respectively. Therefore, PE-ZMOs demonstrated a reduced cliff-like CBO, which benefited the V_{OC} of CZTS/ZTO/PE-ZMO devices. Besides, the device with PE-ZMO 100 had an optimized CBM similar to that of PE-ZMO 150 but a much higher electron concentration, which could benefit both FF and V_{OC} as shown in the theoretical simulation. Therefore, an optimized efficiency can be achieved using ZMO deposited by PE-ALD at 100 °C.

With a better quality of the CZTS absorber layer with a slightly optimized composition (Cu/(Zn+Sn) = 0.88, Zn/Sn = 1.18), the photovoltaic performance of the CZTS/ZTO/PE-ZMO device could be boosted even further, as depicted in Figure S10. The $J-V$ characteristic of the champion solar cell with a PE-ZMO window layer is shown in Figure 5e. J_{SC} of this champion device was measured to be 21.1 mA/cm^2, which was even higher than the 20.5 mA/cm^2 of the champion CZTS/ZTO device with an i-ZnO window layer but without any interface passivation in a previous report.[1] This enhancement indicated the better light harvesting of the PE-ZMO device by using a window layer with a larger band gap and thinner thickness. V_{OC} of the PE-ZMO device was slightly increased from 720 to 728 mV, which can be explained by a reduced cliff-like CBO between the buffer and window layer. By carefully tuning the optoelectrical properties of the ZMO layer, the PE-ZMO device showed a higher FF of 65.0% than the previous champion device, thereby achieving an improved efficiency of 10.0%.

ALD ZnMgO window layers with controlled thickness, composition, and electro-optical properties were explored in this work. *In situ* ellipsometry measurements revealed the different growth behaviors for ZMOs deposited by T-ALD and PE-ALD due to the different reactivities of the oxidant. Consequently, the resulting thin films exhibited quite different crystalline structures, surface morphologies, and optical and electrical properties. An amorphous ZMO deposited by low-temperature PE-ALD showed smoothness superior to that of high-temperature PE-ALD and doping density comparable to that of high-temperature T-ALD but a much lower work function. The CZTS solar cells with an optimized amorphous ZMO window layer demonstrated a higher efficiency, mainly due to a higher V_{OC} and J_{SC}. EQE in the wavelength region of 350−450 nm was notably enhanced when a larger bandgap of PE-ZMO 100 (3.59 eV) was used, leading to increased J_{SC}. The decreased interface recombination was correlated with the better overall band alignment at the CZTS/ZnSnO/ZnMgO region, thereby contributing to the V_{OC} and FF of CZTS/ZTO/PE-ZMO devices. Finally, a champion 10.0% efficient PE-ZMO device was demonstrated with a device structure of Mo/CZTS/ZnSnO/ZnMgO/ITO. This low-temperature PE-ALD process, together with the *in situ* ellipsometry analysis, demonstrates its capabilities in realizing high-efficiency chalcogenide solar cells and its potential for broad optoelectrical applications.

■ ASSOCIATED CONTENT

Supporting Information

The Supporting Information is available free of charge at https://pubs.acs.org/doi/10.1021/acsmaterialslett.2c01203.

Experimental details, optical data, ellipsometry data, Raman spectra, GIXRD patterns, XPS data, EQE, $J-V$ data, and details of the numerical simulation (PDF)

■ AUTHOR INFORMATION

Corresponding Authors

Kaiwen Sun − *School of Photovoltaic and Renewable Energy Engineering, UNSW Sydney, Sydney, New South Wales 2052,*

https://doi.org/10.1021/acsmaterialslett.2c01203
ACS Materials Lett. 2023, 5, 1456−1465

Australia; orcid.org/0000-0001-5589-226X;
Email: kaiwen.sun@unsw.edu.au

Bram Hoex − *School of Photovoltaic and Renewable Energy Engineering, UNSW Sydney, Sydney, New South Wales 2052, Australia;* orcid.org/0000-0002-2723-5286;
Email: b.hoex@unsw.edu.au

Xiaojing Hao − *School of Photovoltaic and Renewable Energy Engineering, UNSW Sydney, Sydney, New South Wales 2052, Australia;* orcid.org/0000-0001-5903-4481;
Email: xj.hao@unsw.edu.au

Authors

Xin Cui − *School of Photovoltaic and Renewable Energy Engineering, UNSW Sydney, Sydney, New South Wales 2052, Australia;* orcid.org/0000-0003-1973-2060

Jialiang Huang − *School of Photovoltaic and Renewable Energy Engineering, UNSW Sydney, Sydney, New South Wales 2052, Australia*

Heng Sun − *School of Photovoltaic and Renewable Energy Engineering, UNSW Sydney, Sydney, New South Wales 2052, Australia*

Ao Wang − *School of Photovoltaic and Renewable Energy Engineering, UNSW Sydney, Sydney, New South Wales 2052, Australia*

Xiaojie Yuan − *School of Photovoltaic and Renewable Energy Engineering, UNSW Sydney, Sydney, New South Wales 2052, Australia*

Martin Green − *School of Photovoltaic and Renewable Energy Engineering, UNSW Sydney, Sydney, New South Wales 2052, Australia;* orcid.org/0000-0002-8860-396X

Complete contact information is available at:
https://pubs.acs.org/10.1021/acsmaterialslett.2c01203

Author Contributions

X.C. conceived and designed all the experimental work. X.C. and K.S. were involved in CZTS device fabrications. X.C., J.H., A.W., X.Y., and H.S. were involved in material and device characterizations. The manuscript was written by X.C., K.S., B.H., and X.H. All authors contributed to the discussion of the data, writing of the sections of the manuscript, and revision of the manuscript. The overall project was supervised by M.G., B.H., and X.H. CRediT: **Kaiwen Sun** investigation, methodology, writing-review & editing; **xiaojie yuan** methodology; **Martin A. Green** funding acquisition, resources, supervision, writing-review & editing; .

Author Contributions

CRediT: **Xin Cui** conceptualization, investigation, methodology, software, writing-original draft, writing-review & editing; **Kaiwen Sun** investigation, methodology, writing-review & editing; **Jialiang Huang** investigation, methodology, writing-review & editing; **Heng Sun** methodology; **Ao Wang** methodology; **Xiaojie yuan** methodology; **Martin A. Green** funding acquisition, resources, supervision, writing-review & editing; **Bram Hoex** funding acquisition, resources, supervision, writing-review & editing; **Xiaojing Hao** funding acquisition, project administration, resources, supervision, validation, writing-review & editing.

Notes

The authors declare no competing financial interest.

■ ACKNOWLEDGMENTS

This work has been financially supported by the Australian Government through the Australian Renewable Energy Agency (ARENA) (1-USO028), Australian Research Council (ARC). X.H. acknowledges financial support by the Australian Research Council (ARC) Future Fellowship (FT190100756). X.C. acknowledges the Australian Centre for Advanced Photovoltaics (ACAP) postdoctoral fellowship programme (RG193402-A). Responsibility for the views, information, or advice expressed herein is not accepted by the Australian Government. We acknowledge the use of facilities at the Electron Microscope Unit (EMU), The University of New South Wales (UNSW). We acknowledge the scientific and technical assistance for the XPS and UPS measurements at the Surface Analysis Laboratory at Mark Wainwright Analytical Centre, The University of New South Wales (UNSW).

■ REFERENCES

(1) Cui, X.; Sun, K.; Huang, J.; Lee, C.-Y.; Yan, C.; Sun, H.; Zhang, Y.; Liu, F.; Hossain, M. A.; Zakaria, Y.; et al. Enhanced Heterojunction Interface Quality To Achieve 9.3% Efficient Cd-Free Cu2ZnSnS4 Solar Cells Using Atomic Layer Deposition ZnSnO Buffer Layer. *Chem. Mater.* **2018**, *30*, 7860−7871.

(2) Cui, X.; Sun, K.; Huang, J.; Yun, J. S.; Lee, C.-Y.; Yan, C.; Sun, H.; Zhang, Y.; Xue, C.; Eder, K. Cd-Free Cu2ZnSnS4 solar cell with an efficiency greater than 10% enabled by Al2O3 passivation layers. *Energy Environ. Sci.* **2019**, *12*, 2751−2764.

(3) Yan, C.; Huang, J.; Sun, K.; Johnston, S.; Zhang, Y.; Sun, H.; Pu, A.; He, M.; Liu, F.; Eder, K.; et al. Cu2ZnSnS4 solar cells with over 10% power conversion efficiency enabled by heterojunction heat treatment. *Nature Energy* **2018**, *3*, 764−772. Sun, K.; Yan, C.; Huang, J.; Liu, F.; Li, J.; Sun, H.; Zhang, Y.; Cui, X.; Wang, A.; Fang, Z.; et al. Beyond 10% efficiency Cu 2 ZnSnS 4 solar cells enabled by modifying the heterojunction interface chemistry. *Journal of Materials Chemistry A* **2019**, *7*, 27289−27296.

(4) Ishizuka, S.; Sakurai, K.; Yamada, A.; Matsubara, K.; Fons, P.; Iwata, K.; Nakamura, S.; Kimura, Y.; Baba, T.; Nakanishi, H.; et al. Fabrication of wide-gap Cu(In1−xGax)Se2 thin film solar cells: a study on the correlation of cell performance with highly resistive i-ZnO layer thickness. *Sol. Energy Mater. Sol. Cells* **2005**, *87*, 541−548.

(5) Platzer-Björkman, C. *Band alignment between ZnO-based and Cu (In, Ga) Se2 thin films for high efficiency solar cells*; Acta Universitatis Upsaliensis: 2006.

(6) Löckinger, J.; Nishiwaki, S.; Weiss, T. P.; Bissig, B.; Romanyuk, Y. E.; Buecheler, S.; Tiwari, A. N. TiO 2 as intermediate buffer layer in Cu(In,Ga)Se 2 solar cells. *Sol. Energy Mater. Sol. Cells* **2018**, *174*, 397−404.

(7) Troni, F.; Sozzi, G.; Menozzi, R. *A numerical study of the design of ZnMgO window layer for Cadmium-free thin-film CIGS solar cells*; IEEE: 2011. DOI: 10.1109/prime.2011.5966250.

(8) Chantana, J.; Kato, T.; Sugimoto, H.; Minemoto, T. Structures of Cu (In, Ga)(S, Se) 2 solar cells for minimizing open-circuit voltage deficit: Investigation of carrier recombination rates. *Progress in Photovoltaics: Research and Applications* **2019**, *27*, 630−639.

(9) Ablekim, T.; Colegrove, E.; Metzger, W. K. Interface engineering for 25% CdTe solar cells. *ACS Applied Energy Materials* **2018**, *1*, 5135−5139.

(10) Munshi, A. H.; Kephart, J. M.; Abbas, A.; Shimpi, T. M.; Barth, K. L.; Walls, J. M.; Sampath, W. S. Polycrystalline CdTe photovoltaics with efficiency over 18% through improved absorber passivation and current collection. *Sol. Energy Mater. Sol. Cells* **2018**, *176*, 9−18.

(11) Nakamura, M.; Yamaguchi, K.; Kimoto, Y.; Yasaki, Y.; Kato, T.; Sugimoto, H. Cd-free Cu (In, Ga)(Se, S) 2 thin-film solar cell with record efficiency of 23.35%. *IEEE J. Photovoltaics* **2019**, *9*, 1863−1867.

(12) Minemoto, T.; Negami, T.; Nishiwaki, S.; Takakura, H.; Hamakawa, Y. Preparation of Zn1− xMgxO films by radio frequency magnetron sputtering. *Thin Solid Films* **2000**, *372*, 173−176.
(13) Makino, T.; Segawa, Y.; Kawasaki, M.; Ohtomo, A.; Shiroki, R.; Tamura, K.; Yasuda, T.; Koinuma, H. Band gap engineering based on MgxZn1−xO and CdyZn1−yO ternary alloy films. *Appl. Phys. Lett.* **2001**, *78*, 1237−1239.
(14) Liu, W.; Gu, S.; Zhu, S.; Ye, J.; Qin, F.; Liu, S.; Zhou, X.; Hu, L.; Zhang, R.; Shi, Y.; et al. The deposition and annealing study of MOCVD ZnMgO. *J. Cryst. Growth* **2005**, *277*, 416−421.
(15) Platzer-Björkman, C.; Törndahl, T.; Hultqvist, A.; Kessler, J.; Edoff, M. Optimization of ALD-(Zn,Mg)O buffer layers and (Zn,Mg)O/Cu(In,Ga)Se2 interfaces for thin film solar cells. *Thin Solid Films* **2007**, *515*, 6024−6027.
(16) Bendersky, L.; Takeuchi, I.; Chang, K.-S.; Yang, W.; Hullavarad, S.; Vispute, R. Microstructural study of epitaxial Zn 1− x Mg x O composition spreads. *J. Appl. Phys.* **2005**, *98*, 083526.
(17) Chen, W.; Pan, X.; Zhang, H.; Ye, Z.; Ding, P.; Chen, S.; Huang, J.; Lu, B. Small valence band offsets of non-polar ZnO/Zn1− xMgxO heterojunctions measured by X-ray photoelectron spectroscopy. *Phys. Lett. A* **2014**, *378*, 2312−2316. Yin, H.; Chen, J.; Wang, Y.; Wang, J.; Guo, H. Composition dependent band offsets of ZnO and its ternary alloys. *Sci. Rep.* **2017**, *7*, 41567.
(18) Ke, Y.; Berry, J.; Parilla, P.; Zakutayev, A.; O'Hayre, R.; Ginley, D. The origin of electrical property deterioration with increasing Mg concentration in ZnMgO: Ga. *Thin Solid Films* **2012**, *520*, 3697−3702.
(19) Chantana, J.; Kato, T.; Sugimoto, H.; Minemoto, T. Thin-film Cu (In, Ga)(Se, S) 2-based solar cell with (Cd, Zn) S buffer layer and Zn1− xMgxO window layer. *Progress in Photovoltaics: Research and Applications* **2017**, *25*, 431−440.
(20) Rajbhandari, P. P.; Bikowski, A.; Perkins, J. D.; Dhakal, T. P.; Zakutayev, A. Combinatorial sputtering of Ga-doped (Zn,Mg)O for contact applications in solar cells. *Sol. Energy Mater. Sol. Cells* **2017**, *159*, 219−226. Chantana, J.; Kawano, Y.; Nishimura, T.; Kimoto, Y.; Kato, T.; Sugimoto, H.; Minemoto, T. 22%-efficient Cd-free Cu(In,Ga)(S,Se) 2 solar cell by all-dry process using Zn 0.8 Mg 0.2 O and Zn 0.9 Mg 0.1 O:B as buffer and transpa. *Progress in Photovoltaics: Research and Applications* **2020**, *28*, 79−89.
(21) Hironiwa, D.; Chantana, J.; Sakai, N.; Kato, T.; Sugimoto, H.; Minemoto, T. Application of multi-buffer layer of (Zn,Mg)O/CdS in Cu2ZnSn(S,Se)4 solar cells. *Curr. Appl. Phys.* **2015**, *15*, 383−388.
(22) Asundi, A. S.; Raiford, J. A.; Bent, S. F. Opportunities for atomic layer deposition in emerging energy technologies. *ACS Energy Letters* **2019**, *4*, 908−925.
(23) Thomas, M. A.; Cui, J. B. Highly tunable electrical properties in undoped ZnO grown by plasma enhanced thermal-atomic layer deposition. *ACS Appl. Mater. Interfaces* **2012**, *4*, 3122−3128.
(24) Zhang, J.; Yang, H.; Zhang, Q.-l.; Dong, S.; Luo, J. K. Structural, optical, electrical and resistive switching properties of ZnO thin films deposited by thermal and plasma-enhanced atomic layer deposition. *Appl. Surf. Sci.* **2013**, *282*, 390−395. Jin, M.-j.; Jo, J.; Neupane, G. P.; Kim, J.; An, K.-S.; Yoo, J.-W. Tuning of undoped ZnO thin film via plasma enhanced atomic layer deposition and its application for an inverted polymer solar cell. *AIP Advances* **2013**, *3*, 102114.
(25) Vangelista, S.; Mantovan, R.; Lamperti, A.; Tallarida, G.; Kutrzeba-Kotowska, B.; Spiga, S.; Fanciulli, M. Low-temperature atomic layer deposition of MgO thin films on Si. *J. Phys. D: Appl. Phys.* **2013**, *46*, 485304.
(26) Baji, Z.; Lábadi, Z.; Horváth, Z. E.; Molnár, G.; Volk, J.; Bársony, I.; Barna, P. Nucleation and Growth Modes of ALD ZnO. *Cryst. Growth Des.* **2012**, *12*, 5615−5620.
(27) Van Bui, H.; Wiggers, F. B.; Gupta, A.; Nguyen, M. D.; Aarnink, A. A. I.; De Jong, M. P.; Kovalgin, A. Y. Initial growth, refractive index, and crystallinity of thermal and plasma-enhanced atomic layer deposition AlN films. *J. Vac. Sci. Technol., A* **2015**, *33*, 01A111.
(28) Askeland, D. R.; Wright, W. J. *The Science and Engineering of Materials*, 6th ed.; Cengage: 2010.
(29) Törndahl, T.; Platzer-Björkman, C.; Kessler, J.; Edoff, M. Atomic layer deposition of Zn1−xMgxO buffer layers for Cu(In,Ga)-Se2 solar cells. *Progress in Photovoltaics: Research and Applications* **2007**, *15*, 225−235.
(30) Mackus, A. J. M.; Schneider, J. R.; MacIsaac, C.; Baker, J. G.; Bent, S. F. Synthesis of Doped, Ternary, and Quaternary Materials by Atomic Layer Deposition: A Review. *Chem. Mater.* **2019**, *31*, 1142−1183.
(31) Guc, M.; Hariskos, D.; Calvo-Barrio, L.; Jackson, P.; Oliva, F.; Pistor, P.; Perez-Rodriguez, A.; Izquierdo-Roca, V. Resonant Raman scattering based approaches for the quantitative assessment of nanometric ZnMgO layers in high efficiency chalcogenide solar cells. *Sci. Rep* **2017**, *7*, 1144.
(32) Elam, J.; Sechrist, Z.; George, S. ZnO/Al2O3 nanolaminates fabricated by atomic layer deposition: growth and surface roughness measurements. *Thin Solid Films* **2002**, *414*, 43−55.
(33) Fleischer, K.; Arca, E.; Smith, C.; Shvets, I. Aluminium doped Zn 1− x Mg x O—A transparent conducting oxide with tunable optical and electrical properties. *Appl. Phys. Lett.* **2012**, *101*, 121918.
(34) Matsubara, K.; Tampo, H.; Shibata, H.; Yamada, A.; Fons, P.; Iwata, K.; Niki, S. Band-gap modified Al-doped Zn 1− x Mg x O transparent conducting films deposited by pulsed laser deposition. *Appl. Phys. Lett.* **2004**, *85*, 1374−1376.
(35) Godlewski, M.; Guziewicz, E.; Szade, J.; Wójcik-Głodowska, A.; Krajewski, T.; Kopalko, K.; Jakieła, R.; Yatsunenko, S.; Przeździecka, E.; Kruszewski, P.; et al. Vertically stacked non-volatile memory devices−material considerations. *Microelectron. Eng.* **2008**, *85*, 2434−2438.
(36) Burgelman, M.; Decock, K.; Khelifi, S.; Abass, A. Advanced electrical simulation of thin film solar cells. *Thin Solid Films* **2013**, *535*, 296−301.

https://doi.org/10.1021/acsmaterialslett.2c01203
ACS Materials Lett. 2023, 5, 1456−1465